JOURNAL OF MATERIALS SCIENCE **33** (1998) 313–318

Fracture characteristic of a (Si–Al–O–N)–SiC composite studied by transmission electron microscopy

BYONG-TAEK LEE
Department of Materials Engineering, Kongju National University, 182 Sinkwan-Dong, Kongju City 314-701, South Korea

The microstructure and fracture characteristic of a pressureless-sintered (Si–Al–O–N)–6 wt % SiC composite have been investigated by a combination of transmission electron microscopy and microindentation fracture technique. SiC particles of nanometre size were dispersed in Si–Al–O–N grains and, at grain boundaries, were associated with strong strain fields. Si–Al–O–N grain boundaries were formed with an amorphous layer about 2 nm thick. However, interfaces between Si–Al–O–N and SiC embedded in the Si–Al–O–N grains were directly joined without any amorphous layer. The main fracture mode was an intergranular type, but some transgranular fracture by the dispersion of nanometre-sized SiC in the Si–Al–O–N grains are also observed at the crack wake zone. The fracture toughening mechanisms of crack deflection, bridging and microcracking were not observed in the (Si–Al–O–N)–6 wt % SiC nanocomposite system.

1. Introduction

To improve the mechanical properties, such as fracture strength and toughness, of structural ceramics, the formation of composites by the dispersion of various types of reinforcement has attracted attention [1–3]. It is well known that physical and morphological relationships between matrix and reinforcements (i.e., their thermal expansion coefficients, lattice parameters, crystal structures, shapes and volume fractions) must be considered for ceramic design, since they are related to the mechanical properties. Recently, nanometre-scaled composites, called nanocomposites, in which a few per cent of reinforcements of nanometre size are intragranularly and intergranularly dispersed in the matrix, have been reported for Si_3N_4–SiC composite systems [4, 5].

β-(Si–Al–O–N) ceramic has attracted much attention as a potential material for applications in engine components, because of its high-temperature strength, high oxidation resistance, high chemical stability and low thermal expansion coefficient [6–11]. Recently, Yamagishi *et al.* [12, 13] reported that a nanocomposite was obtained in the Si–Al–O–N system which was fabricated by the pressureless sintering process using high-purity fine β-(Si–Al–O–N) powders. Although there have been a few reports of the transmission electron microscopy (TEM) observations of (Si–Al–O–N)–SiC composites, the relationships between their microstructure and fracture toughening mechanisms have not been significantly investigated until now.

In this work, the microstructure of a (Si–Al–O–N)–6 wt % SiC nanocomposite was examined by high-resolution electron microscopy (HREM). In addition, the fracture behaviour of the (Si–Al–O–N)–6 wt % SiC composite was investigated by the observation of cracks made by Vickers microindentation.

2. Experimental procedure

The (Si–Al–O–N)–6 wt % SiC composite was provided by Nihorn Ceratec Co. Detailed fabrication conditions, for this composite used in this work, have been reported in previous papers [12, 13]. Si–Al–O–N powders with $z = 0.5$ ($Si_{5.5}Al_{0.5}O_{0.5}N_{7.5}$) were prepared by carbon–thermal reduction at 1450 °C for 5 h in a N_2 atmosphere [12]. Starting powders with a nominal composition of β-(Si–Al–O–N)–6 wt % SiC were mixed using a wet ball-mill in a plastic jar. As a sintering additive, 5 wt % Y_2O_3 powders were selected for liquid-phase sintering. These mixed powders were formed into a green body under a pressure of 33 MPa and then sintered in a carbon crucible at 1780 °C for 3 h under a N_2 atmosphere by pressureless sintering. TEM samples for observations of microstructure and fracture behaviour were prepared from thin slices, which had been mechanically polished to a thickness of about 150 μm. Discs of 3 mm diameter were cut out with an ultrasonic cutter. After polishing to a mirror plane, indentations were made with a load of 50 g for 15 s by a Vickers indenter (Akashi MVK-VL). The back side of the indented plane was polished further up to about 30 μm in thickness by a dimple grinder and finally milled with Ar ions at an accelerating voltage of 3 kV. The glancing angle was 25°. Carbon coating was done prior to TEM observations, in

0022–2461

order to prevent charge-up effects. TEM and HREM observations were made with a JEM-4000EX 400 kV electron microscope with a resolution of 0.17 nm. For the characterization of fracture morphology, a JSM-5300 scanning electron microscope was used.

3. Results and discussion

3.1. Characterization of microstructure

Fig. 1 shows a typical TEM image of the (Si–Al–O–N)–6 wt % SiC composite. The average grain size of Si–Al–O–N is about 0.4 μm, which is finer than those reported in other papers [8–11]. However, rod-like grains, which were frequently observed in Si_3N_4 and Si–Al–O–N ceramics, were not observed because its sintering was carried out at a comparatively low temperature (1780 °C). Fine SiC particles were intragranularly and intergranularly dispersed in Si–Al–O–N grains, as indicated by arrowheads. Most of the Si–Al–O–N grains exhibit strain contrast attributed to the dispersion of SiC nanoparticles. The electron diffraction pattern shown as an inset in Fig. 1 was taken from the triple-point region labelled P. In the pattern, a faint ring is seen, in addition to some spots coming from surrounding Si–Al–O–N grains. The pattern indicates that the triple point is constructed with an amorphous phase.

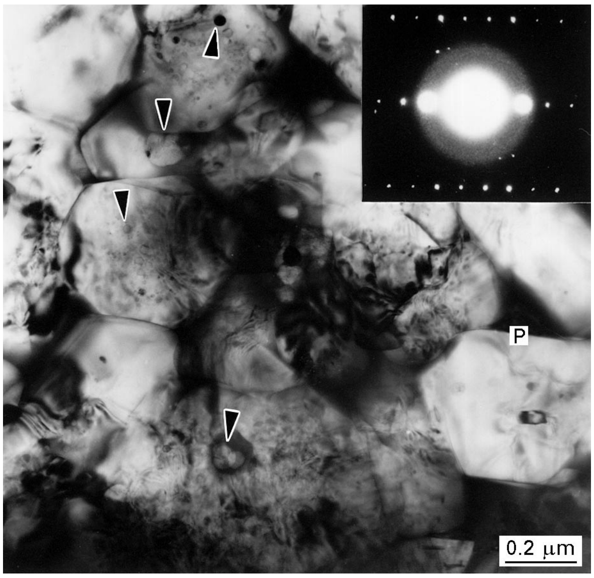

Figure 1 TEM image of a (Si–Al–O–N)–6 wt % SiC composite and an electron diffraction pattern of the triple point labelled P.

The nanometre-sized SiC particles in the Si–Al–O–N grains as seen in Fig. 1, are clearly visualized by specimen tilting. Fig. 2 shows TEM images of the same region, taken with the incident beam slightly tilted. In the micrographs, a few SiC particles with a spherical shape as indicated with arrowheads appear and/or disappear with strain contrasts by the differences in electron diffraction conditions.

Fig. 3 is a HREM image showing a Si–Al–O–N large-angle grain boundary. The image shows one-dimensional lattice images of the (1 0 0) planes in both grains. The existence of a thin amorphous layer about 2 nm thick, as indicated by the white arrows, is clearly shown. Like this, most Si–Al–O–N grain boundaries are constructed with thin amorphous layers, as has been seen in liquid-phase-sintered ceramics [14, 15].

Fig. 4a and b show a HREM image of a SiC particle located at a grain boundary and an enlarged image of the rectangular region in Fig. 4a, respectively. The HREM image in Fig. 4b shows the existence of an amorphous region at the (Si–Al–O–N)–SiC interface. The SiC particle size is about 90 nm, and its crystal structure shows a β-typed cubic structure containing many (1 1 1) twins and stacking faults. The zigzag surface of the SiC particle is caused by the existence of twin defects, which are frequently observed in SiC crystals [15]. The internal defects within SiC particles may arise from when they were formed with SiC raw powder. It is noticed that SiC particles located at Si–Al–O–N grain boundaries were always covered with Y–Si–Al–O–N amorphous phase. Generally, in the liquid-phase-sintered ceramic composites, grain boundaries, interfaces and triple

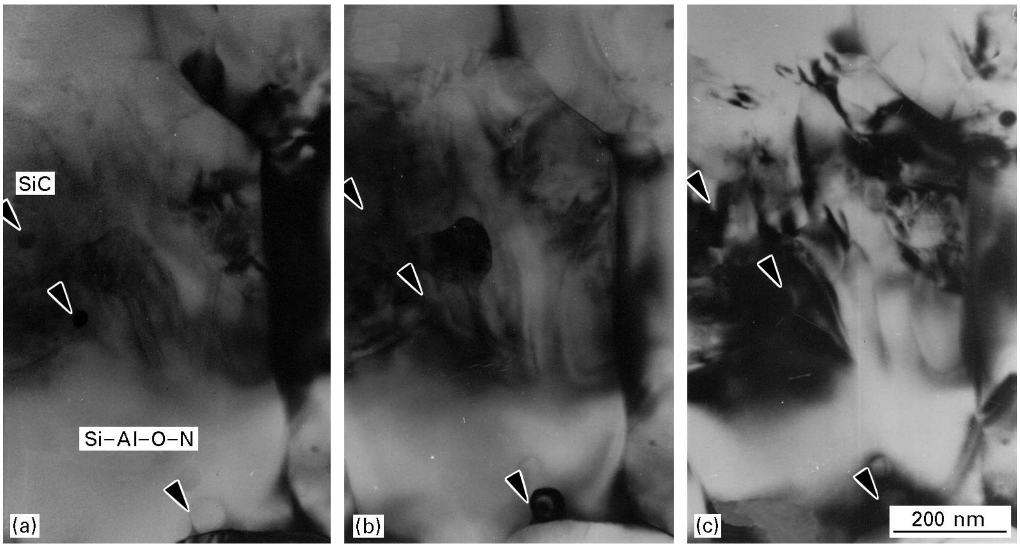

Figure 2 TEM images showing distribution of nanometre-sized SiC particles in a (Si–Al–O–N)–6 wt % SiC composite. The incident beam is slightly tilted from (a) to (c) at the same position.

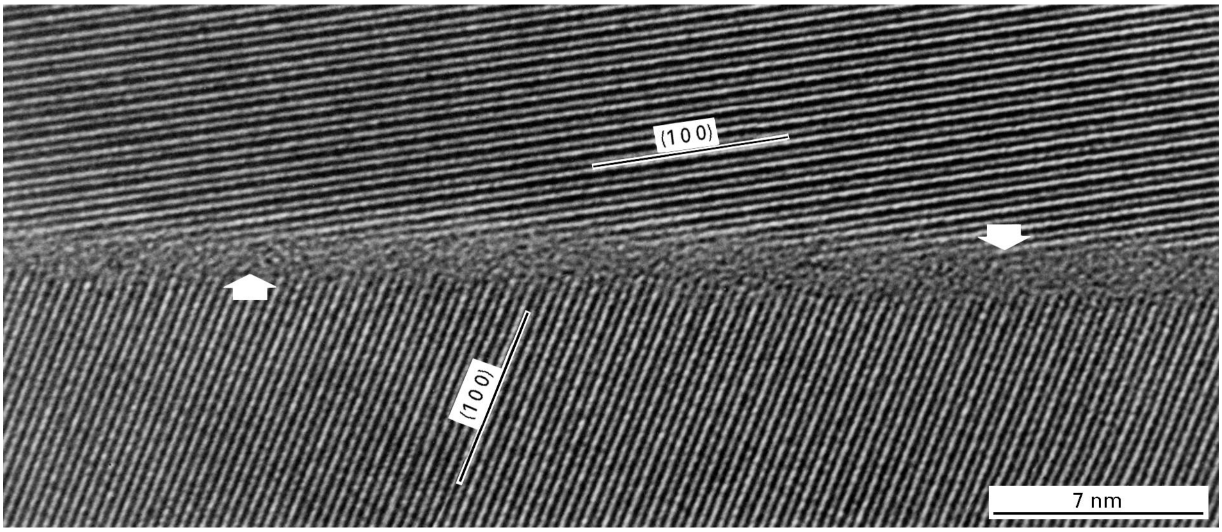

Figure 3 HREM image of a (Si–Al–O–N)–6 wt % SiC composite showing a large-angle grain boundary. The white arrows indicate a thin amorphous layer.

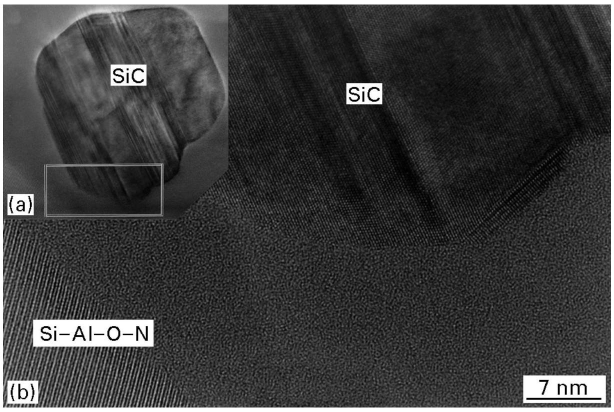

Figure 4 (a) TEM image of a (Si–Al–O–N)–6 wt % SiC composite showing an intergranular SiC particle. (b) HREM image of the rectangular region in (a).

junctions are usually covered with an amorphous phase. In our recent work on Si_3N_4 matrix composites, some amounts of the amorphous phase were observed in the junction region of grains [15]. However, the SiC particles, located inside Si–Al–O–N grains, show interfaces directly bonded without any amorphous phases.

Fig. 5 is a typical HREM image showing a SiC grain embedded in the Si–Al–O–N matrix. At the (Si–Al–O–N)–SiC interface, contrary to Fig. 4, no amorphous layers were observed. The embedded SiC particle has a spherical shape and the crystallographic orientation between $(1\,1\,1)_{\mathrm{SiC}}$ and $(1\,1\,0)_{\mathrm{Si–Al–O–N}}$ is about 156°. Furthermore, in the embedded SiC particles, other internal defects such as the twins and stacking faults observed in Fig. 4 were not observed. From the TEM observation, it is considered that the mechanism of formation of transgranular SiC particles is different from that of SiC particles located at Si–Al–O–N grain boundaries, i.e., the embedded SiC particles may result from the precipitation process because some residual carbon may be retained during the synthesis of raw Si–Al–O–N powders [13].

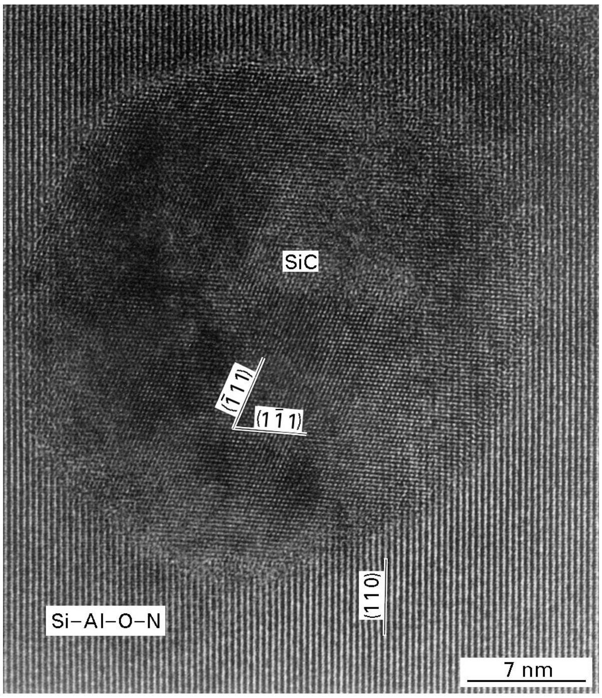

Figure 5 HREM image showing an intragranular SiC particle embedded in Si–Al–O–N matrix.

3.2. Characterization of fracture behaviour

The fracture surface of (Si–Al–O–N)–SiC composites was observed in order to investigate the influence of SiC content on the fracture behaviour. The fracture toughness values of monolithic Si–Al–O–N, (Si–Al–O–N)–6 wt % SiC composite and (Si–Al–O–N)–12 wt % SiC composite were about 4.6 $\mathrm{MPa\,m^{1/2}}$, 5.4 $\mathrm{MPa\,m^{1/2}}$ and 4.8 $\mathrm{MPa\,m^{1/2}}$, respectively, as reported by Yamagishi *et al.* [12, 13]. As shown in Fig. 6, the typical fracture mode changes from intergranular to transgranular fracture with increasing SiC content. Fig. 6a of monolithic Si–Al–O–N shows a typical intergranular fracture surface, whereas Fig. 6b of (Si–Al–O–N)–6 wt % SiC is a mixed-type failure with intergranular and transgranular fractures. The inter-

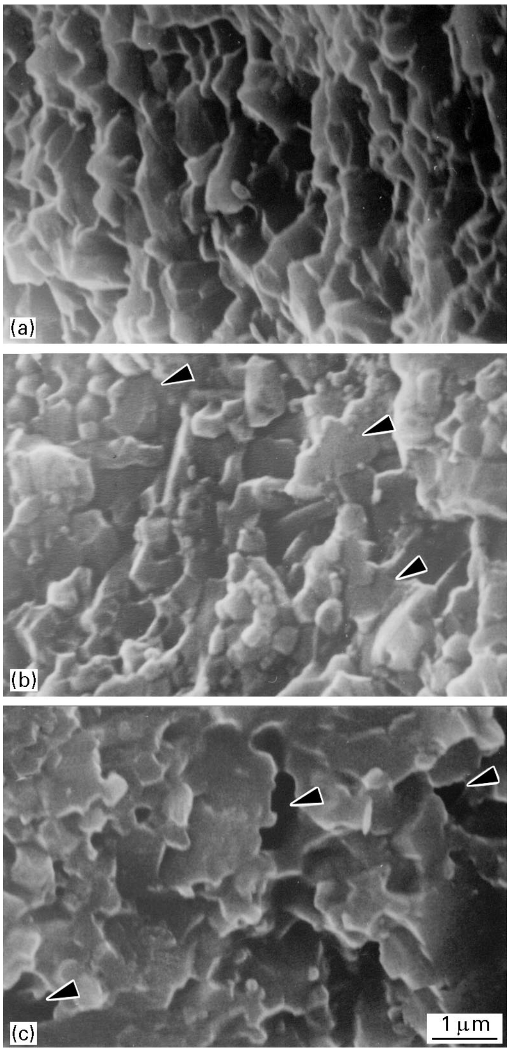

Figure 6 SEM images showing fracture morphologies of (a) monolithic Si–Al–O–N, (b) (Si–Al–O–N)–6 wt % SiC composite and (b) (Si–Al–O–N)–12 wt % SiC composite.

granular type shows sharp grain shapes accompanied by rough surfaces and the transgranular type shows flat cleavage planes as indicated by arrowheads. On the other hand, in (Si–Al–O–N)–12 wt % SiC composite (Fig. 6c), the main fracture mode is transgranular fracture and many residual pores are observed on the fracture surface as indicated by arrowheads. In particular, we cannot observe any crack bridging effect due to the pulling out of Si–Al–O–N grains in these fracture surfaces. Generally, the rod-like grains with large aspect ratio can be obtained using α-type raw Si_3N_4 [14, 15]. This is caused by α- to β-phase transformation, and the rod-like grains are grown along the *c* axis during liquid-phase sintering. In the (Si–Al–O–N)–SiC composites, the absence of a pull-out effect on the fracture surface is caused by the existence of equiaxed β-(Si–Al–O–N) grains as seen in Fig. 1. Furthermore, it is considered that nanometre-sized SiC particles as seen in Figs 1 and 5 do not play an important role in releasing the fracture energy, since their shape and size are compared with those of rod-like Si_3N_4 grain [14, 16] or SiC whiskers [15]. For the clear investigation of microscaled fracture behaviour, i.e., interaction between cracks and SiC particles, we observed the cracks made by microindentation using a 50 g load.

Fig. 7a is a TEM image showing crack propagation in the (Si–Al–O–N)–6 wt % SiC composite. The main crack starts from the indentation labelled I and propagates along Si–Al–O–N grain boundaries, as indicated by arrows. However sometimes, cracks propagated along (Si–Al–O–N)–SiC interfaces, as indicated by arrowheads. The intergranular fracture means that the strength of grain boundaries and interfaces are weaker than that of Si–Al–O–N grains, because their grain boundaries and triple points were constructed with amorphous phase as seen in the HREM images in Figs 3 and 4. However, in the composite, transgranular fracture of Si–Al–O–N grains is also frequently observed in crack wake zones, as shown by a circle in Fig. 7a. The transgranular fracture of Si–Al–O–N crystals is due to the dispersion of SiC nanometre-sized particles in Si–Al–O–N grains. Fig. 7b and c show a HREM image and an electron diffraction pattern, respectively, of encircled region in Fig. 7a, taken from the [0 0 1] incident beam of Si–Al–O–N. From the image, we can see that the Si–Al–O–N grain has a β structure and the crack propagated with a wavy shape through the crystal since the β-(Si–Al–O–N) grain has a strain field due to the dispersion of SiC particles. Lattice distortion near the crack was also observed, as can be seen from some divergent spots observed in the electron diffraction pattern. Fig. 8a shows a part of the crack wake zone, in which a crack transgranularly propagates with curved profile in the Si–Al–O–N grain. This observation indicates that, when cracks propagate into Si–Al–O–N grains, they interact with SiC nanocrystals, i.e., the existence of residual stress in Si–Al–O–N grains as seen in Fig. 2 owing to a lattice mismatch between Si–Al–O–N and SiC causes transgranular fracture of Si–Al–O–N. However, microcracking, which was observed in a previous study of Si_3N_4–TiN and Si_3N_4–ZrO_2 composites [14, 17, 18], is not observed at the crack process zone of (Si–Al–O–N)–6 wt % SiC composite because there is no significant difference between the thermal expansion coefficients of Si–Al–O–N and SiC crystals. However, whenever SiC particles are located at grain boundaries with a comparatively large size (submicron size), a short-range-ordered crack deflection was observed by the intergranular fracture, as seen in Fig. 8b. However, from the viewpoint of fracture toughening, it should be pointed out that the dispersion of nanometre-scaled SiC reinforcements does not give a remarkable reduction in the fracture energy of the (Si–Al–O–N)–6 wt % SiC composite, since there are no significant toughening mechanisms, such as microcracking, crack bridging and deflection, or phase transformation mechanism. The fracture characteristics of the (Si–Al–O–N)–6 wt % SiC composite are consistent with the small improvement in the fracture toughness to about 5.4 $MPa\,m^{1/2}$, which is about half the values for SiC-whisker-, TiN-particle- and ZrO_2-reinforced-Si_3N_4 composites where the multimechanisms [14–19] of microcracking, crack deflection, crack bridging and phase transformation were observed.

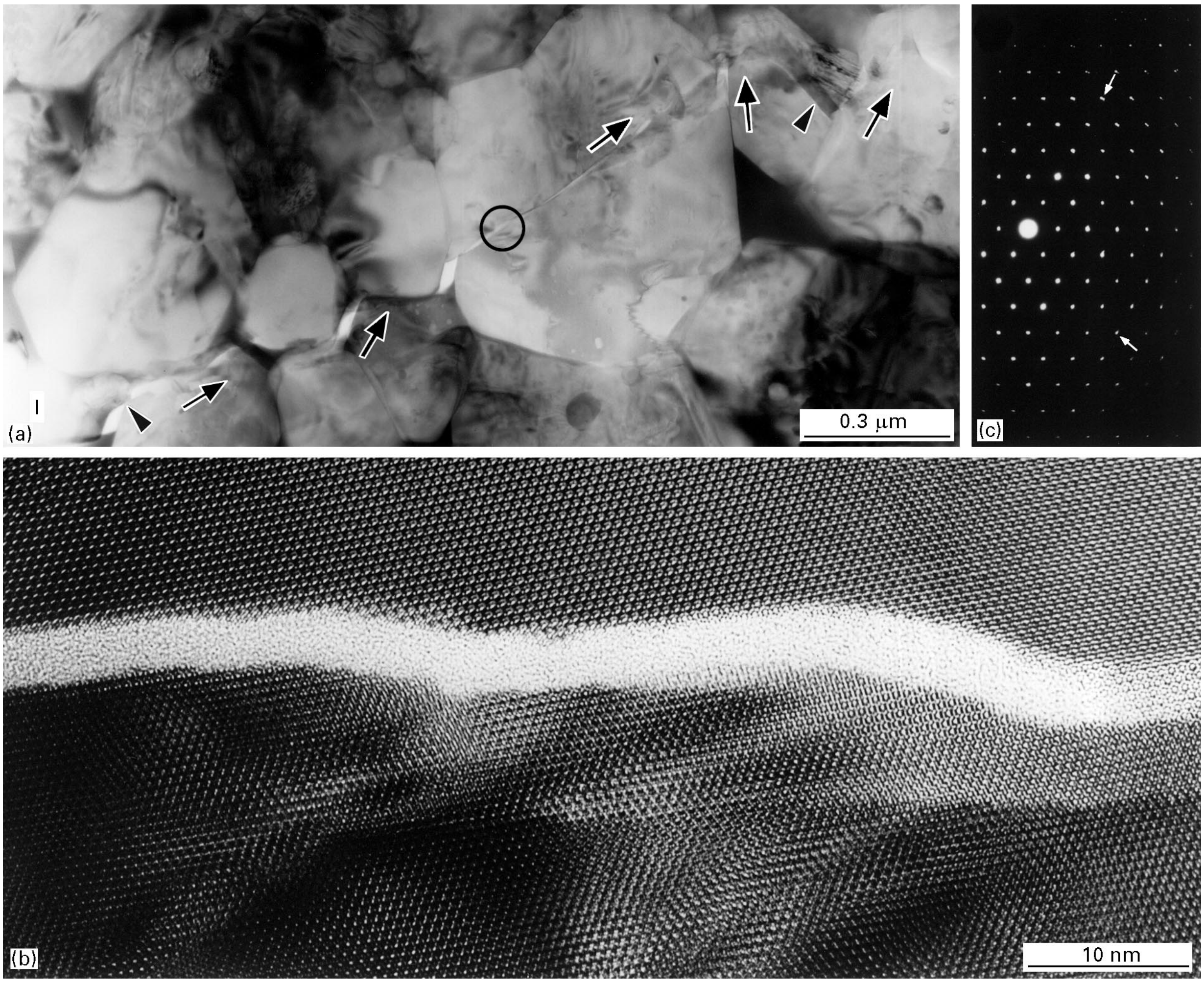

Figure 7 (a) TEM image showing a crack propagation in a (Si–Al–O–N)–6 wt % SiC composite; (b) HREM image of the encircled region in (a); (c) corresponding electron diffraction pattern.

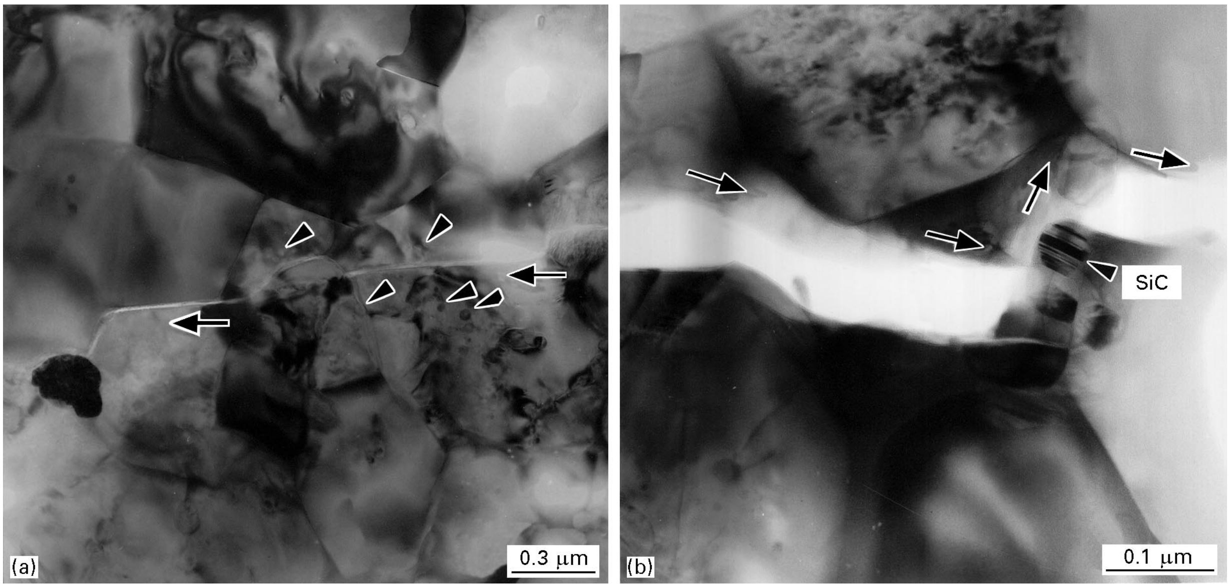

Figure 8 TEM images of a (Si–Al–O–N)–6 wt % SiC composite showing crack propagation of (a) transgranular type and (b) intergranular type. The arrowheads indicate SiC particles.

4. Conclusions

The microstructure and fracture characteristic of the (Si–Al–O–N)–6 wt % SiC composite, prepared by pressureless sintering at 1780 °C, are characterized as follows.

1. Nanometre-sized SiC particles are dispersed in Si–Al–O–N grains and, at grain boundaries, were associated with strain contrast. The structure of Si–Al–O–N grains is β-type hexagonal close packed, and SiC is mainly β-type cubic. As internal defects,

stacking faults and microtwins are observed in intergranular SiC particles, while those defects are not observed in intragranular SiC particles.

2. Most of Si–Al–O–N grain boundaries have a random orientation, and contain an amorphous phase about 2 nm thick. Most triple points have an amorphous phase with a comparatively large region. Interfaces between Si–Al–O–N and SiC embedded in a Si–Al–O–N grain are directly joined without any amorphous layer.

3. The main fracture mode is intergranular type, but frequently transgranular fracture was also observed in Si–Al–O–N grains containing a dispersion of nanometre-sized SiC crystals. Although short-range crack deflection occurs owing to the dispersion of SiC particles, there is no important fracture toughening mechanism associated with this phenomenon.

Acknowledgements

I am grateful to Mr M. Hayashi, Nihorn Ceratec Co. for providing the sample used in the present work, and to Professor K. Hiraga for helpful discussions and for providing research facilities at the Institute for Materials Research, Tohoku University.

References

1. A. TSUGE, K. NISHIDA and M. KOMATSU, *J. Amer. Ceram. Soc.* **58** (1975) 323.
2. F. F. LANGE, *ibid.* **62** (1979) 428.
3. A. G. EVANS, *ibid.* **73** (1990) 187.
4. K. NIIHARA, K. SUGANUMA, A. NAKAHIRA and K. IZAKI, *J. Mater. Sci. Lett.* **9** (1990) 598.
5. A. SAWAGUCHI, K. TODA and K. NIIHARA, *J. Amer. Ceram. Soc.* **74** (1991) 1142.
6. I. B. CUTLER, P. D. MILLER, W. RAFANIELLO and H. K. PARK, *Nature* **275** (1978) 443.
7. W. RAFANIELLO, K. CHO and A. VIRKAR, *J. Mater. Sci.* **16** (1981) 3479.
8. K. KOBAYASHI, S. UMEBAYASHI and K. KISHI, *ibid.* **89** (1981) 550.
9. S. UMEBAYASHI, K. KISHI, E. TANI and K. KOBAYASHI, *ibid.* **92** (1984) 35.
10. H. NAKAMUR, S. UMEBAYASHI and K. KISHI, *J. Ceram. Soc. Jpn.* **98** (1990) 243.
11. K. KISHI, S. UMEBAYASHI, E. TANI, K. KOBAYASHI and H. NAKAMURA, *Yogyo Kyokai Shi* **95** (1987) 450.
12. C. YAMAGISHI, J. HAKOSHIMA, K. TSUKAMOTO and Y. AKIYAMA, *J. Jpn. Soc. Powder Powder Metall.* **37** (1990) 1056.
13. C. YAMAGISHI, K. TSUKAMOTO, J. HAKOSHIMA, H. SHIMOJIMA and Y. AKIYAMA, *J. Mater. Sci.* **27** (1992) 1909.
14. B. T. LEE, T. KOYAMA, A. NISHIYAMA and K. HIRAGA, *Scripta Metall. Mater.* **32** (1995) 1073.
15. B. T. LEE and K. HIRAGA, *Mater. Trans. Jpn. Inst. Metals* **34** (1993) 930.
16. B. T. LEE, G. PEZZOTTI and K. HIRAGA, *Mater. Sci. Engng* **A177** (1994) 151.
17. B. T. LEE, S. HAYASHI, T. HIRAI and K. HIRAGA, *Mater. Trans. Jpn. Inst. Metals* **34** (1993) 573.
18. B. T. LEE and H. D. KIM, *J. Kor. Ceram. Soc.* **33** (1996) 686.
19. B. T. LEE and K. HIRAGA, *J. Mater. Res.* **9** (1994) 1199.

Received 24 February
and accepted 19 August 1997